Characterisation of Landslide using InSAR Technique and Electrical Resistivity Method at Paya Terubong, Malaysia

Kazeem Olukunle Rauff[1] · Ismail Ahmad Abir[1] · Daniele Perissin[2]

Abstract

Ground movement is common around hilly areas; as such, there is a need to investigate the activities of the ground surface and subsurface of such regions. This research presents an application of the Permanent Scatterer Interferometric Synthetic Aperture Radar (PS-InSAR) technique and electrical resistivity (ER) method for the measurement of ground deformations and investigation of the subsurface features, respectively, at Paya Terubong, Penang Island. The PS-InSAR is an instrument for detecting patterns of deformation over a wide region, while the ER approach is used to image subsurface characteristics and measure the resistivity of the rock formation. Satellite data obtained from Sentinel-1A (S-1A) were used to detect some active ground deformation zones. The velocity of − 41 mm/Yr was discovered along the line of sight (LOS) of the system, indicating subsidence. An ER survey was performed at the topsoil within 5 m depth based on the ground deformation patterns detected through the InSAR technique. Two-dimensional (2-D) resistivity lines were laid using the ABEM SAS4000 Terameter and a dipole–dipole array with an electrode spacing of 2.5 m. The areas with low values of resistivity ranging between 0 and 20 Ωm were classified as saturated zones. The efflux and influx of subsurface water when the layers of rocks are lubricated and downcutting of steep slopes are among the suspected causes of deformation. The application of the two techniques has improved the understanding of both the surface and subsurface mechanisms, reduced variation in the results, and allowed the investigation of active landslide areas.

Keywords Ground movement · Subsurface · Electrical resistivity · InSAR technique · Ground deformation

Introduction

Landslide is a natural geohazard that is induced by the action of gravity (Kavzoglu et al. 2014), crashes down without notice, and travels several kilometres. It can cause significant destruction to lives and property globally (Kundu et al. 2013; Di Martire et al. 2016). The two main classifications of landslides are the nature of the movement and the type of materials involved. The movement includes rockfall, internal debris flow, and mudflow that takes place (Schulz et al. 2017) while the materials involved are solid rock or unconsolidated sediments (Furuichi et al. 2018) that are weaker sediments, which have not been compressed considerably by overlying materials (Tappenden 2014). A landslide can either be triggered by natural phenomena such as the action of gravity, snow melting, and continuous rainfall (Mostafa 2012) or by human-made activities such as extraction of oil from the ground, lateral slope cutting for buildings, and movements of human activities (Virk et al. 2019). When it happens, the implications reflect the number of events, like, the presence of people, constructed roads and buildings, and agricultural farming in the environment (Chen et al. 2017).

Table 1 presents some of the past landslide events in different areas of Penang Island between 2016 and 2019. The causes of the hazard, magnitude of the disaster, and district areas they fall in are also shown in the table. The

✉ Kazeem Olukunle Rauff
   rauffkazeem@yahoo.com

   Ismail Ahmad Abir
   iahmadabir@usm.my

   Daniele Perissin
   perissin@purdue.edu

1 School of Physics, Universiti Sains Malaysia,
   11800 Penang Island, USM, Malaysia

2 School of Civil Engineering, Purdue University, Purdue,
   USA

Table 1 Past landslide events

Date	Areas	Coordinate	Disasters	Causes	Districts
14/10/2016	Tanjung Bungah	Lat. 5.465203°, Long. 100.282112°	Roads and buildings were damaged	Heavy rain and flash floods	Northeast
29/10/2016	Air Itam	Lat. 5.402946°, Long. 100.278992°	A car and nine people were trapped in a temple. Hundreds of houses including a village were inundated	Heavy rainstorm	Northeast
1/11/2016	Batu Maung.	Lat. 5.283818°, Long. 100.290036°	More than 100 houses were flooded	Flash-flood and heavy rainfall	Southwest
7/11/2016	Teluk Bahang	Lat. 5.457229°, Long. 100.213573°	The main road in Bahang was closed	Flash floods	Southwest
14/7/2017	Bayan Lepas	Lat. 5.295030°, Long. 100.259172°	One life was lost	Flash floods	Southwest
14/7/2017	Paya Terubong	Lat. 5.374089°, Long. 100.277868°	Hillside Temple was buried	Flash floods	Northeast
15/8/2017	Teluk Bahang	Lat. 5.465203°, Long. 100.282112°	Many properties were destroyed	Flash floods	Northeast
15/9/2017	George Town and other various places	Lat. 5.414825°, Long. 100.328906°	Several cars were seen floating, while some vehicles were damaged	Heavy rain	Northeast
21/9/2017	Paya Terubong	Lat. 5.374089°, Long. 100.277868°	Trees toppled and several main roads were shutdown	Heavy rain	Northeast
5/10/2017	Penang Hills	Lat. 5.408712°, Long. 100.277215°	Two funicular trains got stuck. Mounds and boulders damaged rain track and hauling cables, respectively	Flash-flood and heavy rainfall	Northeast
21/10/2017	Tanjung Bungah	Lat. 5.465203°, Long. 100.282112°	Eleven workers were buried alive by the earth	Flash floods and heavy rain	Northeast
4/11/2017	Tanjung Bungah	Lat. 5.465203°, Long. 100.282112°	A retaining wall was collapsed	Continuous heavy rainfall	Northeast
5/1/2018	Tanjung Bungah	Lat. 5.465203°, Long. 100.282112°	Pepper farm was damaged and four people were trapped therein	Heavy rain caused flash floods	Northeast
11/10/2018	Bukit Kukus	Lat. 5.385189°, Long. 100.279063°	14 concrete beams measuring 25 m each, were collapsed on the hillside	Heavy rain and strong winds	Northeast
19/10/2018	George Town	Lat. 5.414825°, Long. 100.328906°	Nine people lost their lives	A weighty rain	Northeast
25/6/2019	Batu Feringghi	Lat. 5.465203°, Long. 100.282112°	Four foreign workers were buried alive at a construction site in	Flash floods and torrential downpour	Northeast

Penang flash-flood in 2017 was a rare catastrophe that the residents will never forget. The island was collapsed by the worst flash floods ever and heavy rainfall that triggered the extraordinary magnitude of the landslide cases. The affected areas include Penang Hills, Paya Terubong, Batu Ferringhi, Tanjung Bungah, etc. These landslides became active and prompted the slope in these regions to shift. Figure 1 shows a few disasters of the landslide occurrences

Fig. 1 Landslides activities of Penang Hills (**a–c**), the landslides, and downpour that caused more than 100 homes inundated in Penang (**d**) and The Tanjung Bungah landslide and Paya Terubong (**e**)
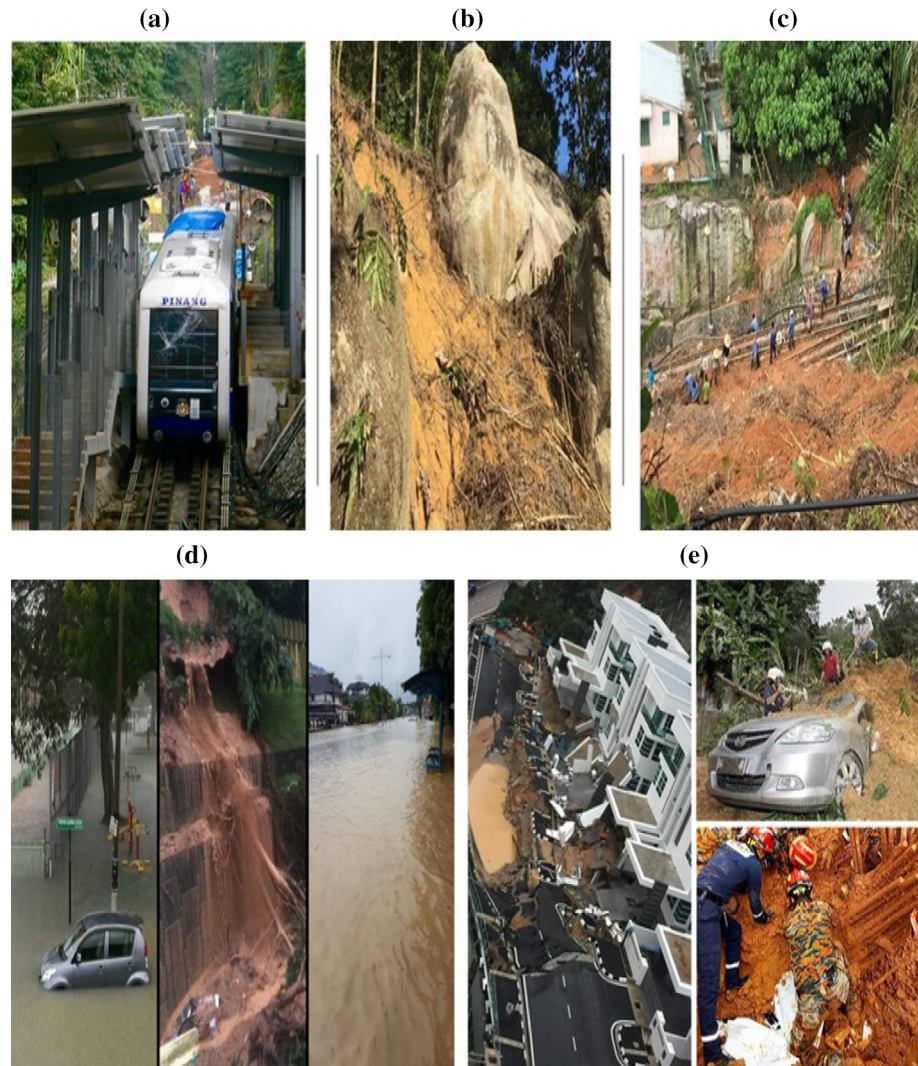
due to these torrential rains that caused rock surface failure across a joint, fracture, and cleavage planes. One of the incidents was a landslide due to massive rain and winds that struck Penang Hills, a world-famous heritage landmark on 5th October 2017. Train operations were disrupted as earth mounds sunk near the middle station on the trail, and many assets such as transport cables and two funicular trains were lost. Also, around 4th and 5th November 2017, the island experienced an extreme storm that caused numerous landslides that damaged lives and property in Penang Island (Pradhan and Lee 2010).

This research is aimed at applying the technique of PS-InSAR to measure ground deformations and ER to characterise underground water distribution, spatial stratigraphy, and material properties. The objectives include detecting ground surface displacements, imaging subsurface structures, and investigating saturated zones, and finally validating the output using borehole data. The

in situ measurement for this study was carried at Paya Terubong, Malaysia, in 2019.

Study Area

This study was performed in Penang Island, northwest of Peninsular Malaysia, with the geographical coordinate (05° 41′ 64″ N, 100° 33′ 22″ E) as presented in Figs. 1b and 2a. Penang is a developed state, and its growth and industrialisation draw people worldwide (Paradella et al. 2015). The area is vulnerable to severe incidents such as subsidence, landslides, and collapse of human-made buildings because of the hilly nature of the region coupled with the highest rainfall of 647 cm per year (Gin 2015). Road cuts for modern buildings and deforestation activities on hills coupled with natural erosion are the leading causes of soil instability in the area (Chee et al. 2017). Paya Terubong is
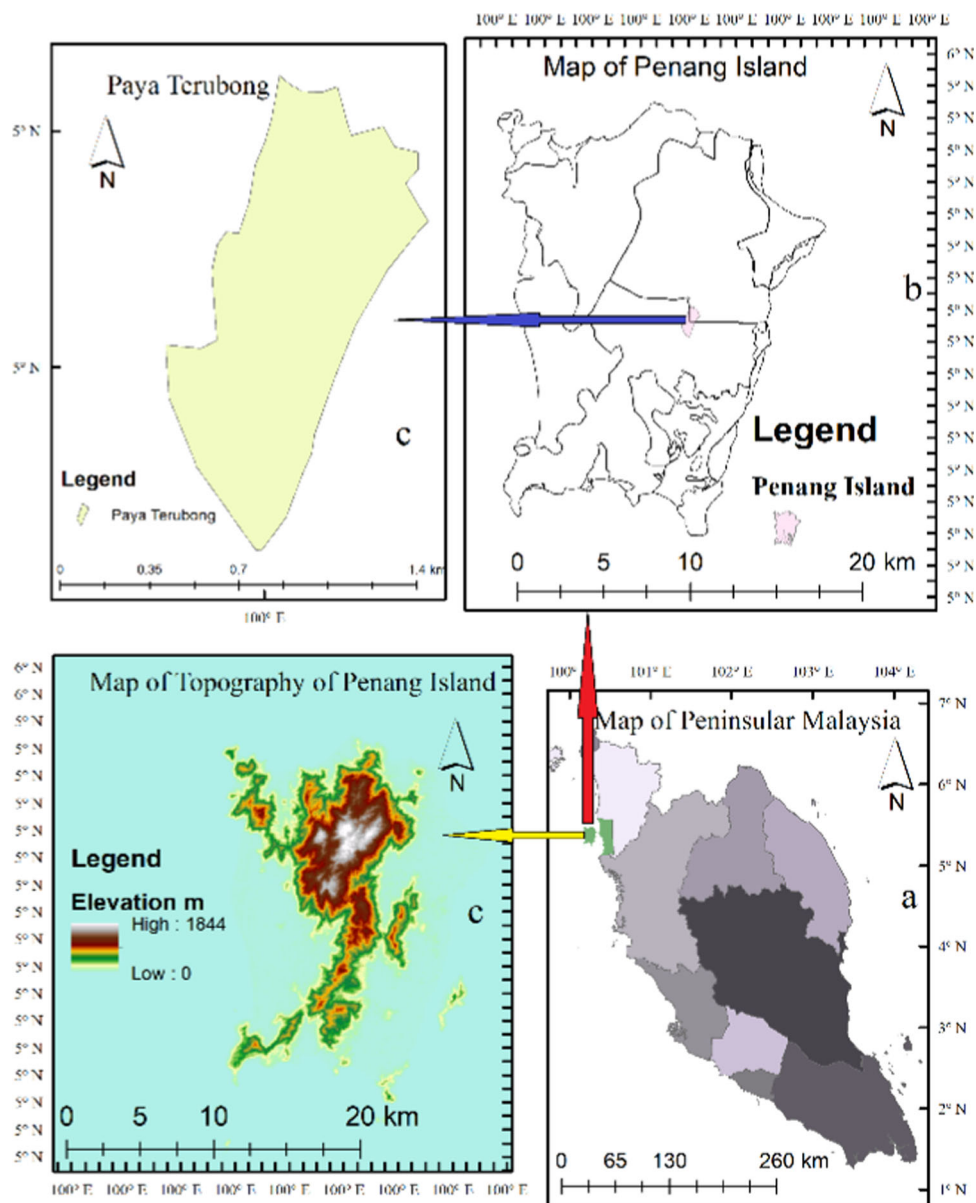
used as the study site for in situ measurement, as depicted in Fig. 2c. The topography of the area based on the digital elevation model is shown in Fig. 2d. The elevation ranges from 700 to 1000 m above sea level (asl) with the highest in the northern part, and lowest in the western region, along the road. The instability in the topography correlates with the boundary of the two classes of granite that makes up the island.

Geology of Penang Island

The knowledge of the geology of the study area cannot be overlooked. It is used in the resistivity analysis for the investigation of the subsurface activities (Ahmad et al.

2006). Penang Island is relatively stable and underlain by an igneous type of rock when classified based on the fraction of compositions of alkali feldspar to total feldspars, as shown in Fig. 3 (Kwan et al. 1992; Wilkinson et al. 2014). It consists of two districts, namely Northeast and Southwest, as illustrated in Table 1, and the geological status of the two regions differs though they are in the same state. Forty per cent of the northeastern part of the island is covered by the intermediate microcline granite (Ahmad et al. 2006). This granite is divided into three units, namely Ferringhi granite, Tanjung Bungah granite, and Muka Head microgranite, as shown in Fig. 3. These units display crustal interactions split by shear zones, faults, and veins. The southern part consists of a gentle slope with an average height of 360 m asl, covered by microcline granite, which

Fig. 3 Map of the geology of Penang Island
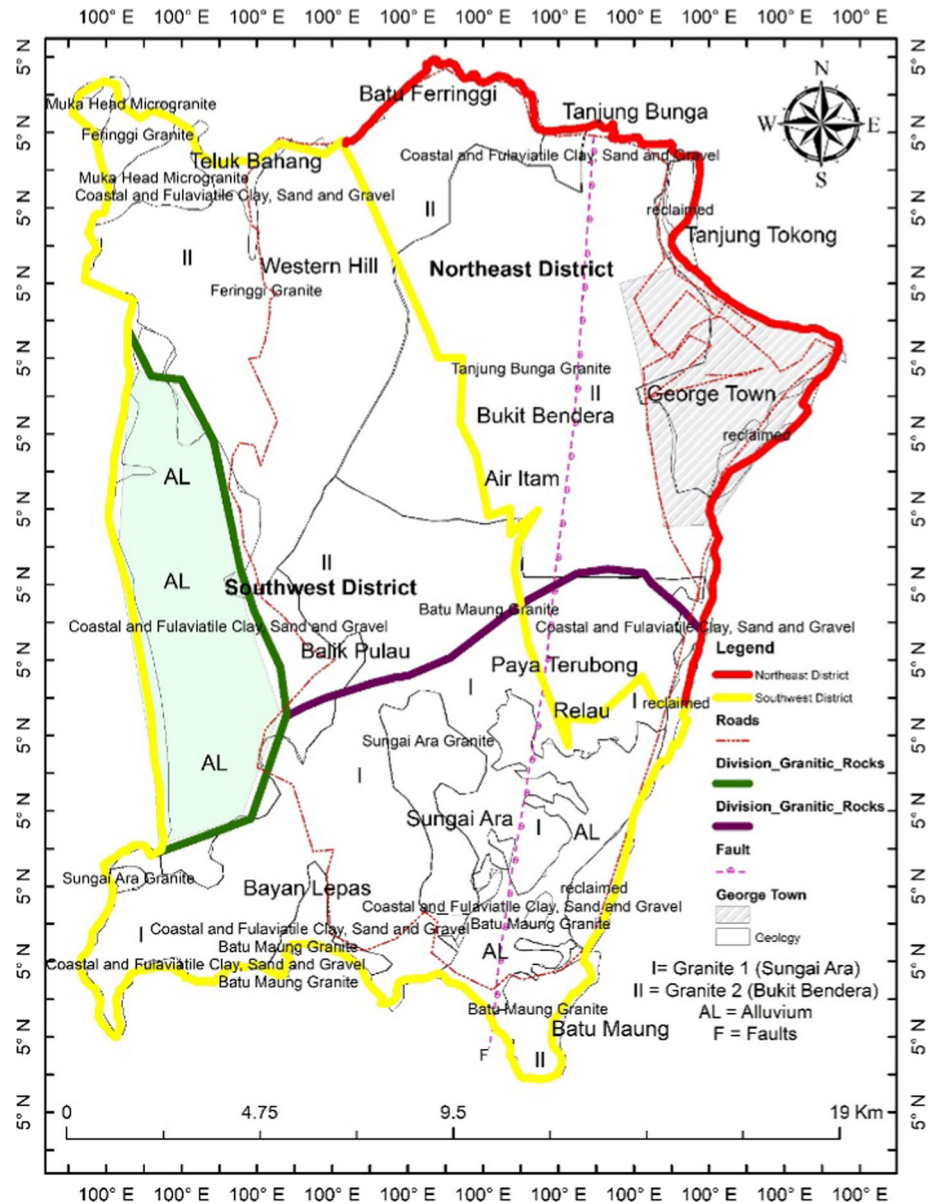
is divided into Batu Maung and Sungai Ara granites, as presented in the same Fig. 3. Eighty per cent of this southern part is covered by Batu Maung granites (e.g. megacrysts), while the remaining twenty per cent is covered by the Sungai Ara granites. The alluvial deposit comprises clay, sand, gravel, and silt clay up to 20 m deep, and dominates the western region of the island (Hassan et al. 2018).

Soil Properties

Understanding the characteristics of the soil sequence is essential to classify its impacts. The soil series of Penang Island is composed of residual soil as categorised under granitic soils with an average of dry density varying between 1.41 and 2.31 kkN/m^3 and depth to bedrock ranging from 2.41 to 40 m (Ahmad et al. 2006). This soil series is formed by the deposit of organic material that is not transported. The soil series of Penang Island is classified into eight types, as follows Steep land, Urban land, Serong, Rengam, Local alluvium–colluvium association, Kuala-Kedah Permatang association, Selangor Kangkong association, and Rengam Bukit Demian association (Pradhan and Lee 2010). The steep soil type dominates the major part of the island, and this is where most of the landslide accidents have been reported (Ali et al. 2011). The distribution of the soil series of the study area is presented in Table 2. Penang Island consists of two types of

Table 2 Series of main soils of Penang Island (Pradhan and Lee 2010)

Area	Size of Grain	Texture
Paya Terubong	Medium to coarse-grained biotite granite with microcline	Sand, gravel, silt, and clay
Batu Ferringhi	Medium to coarse-grained biotite granite with orthoclase to intermediate microcline	Sand, gravel, silt, and clay
Tanjung Bungah	Fine to coarse-grained biotite granite with orthoclase to intermediate microcline	Gravel, sand, silt, and clay

granite rocks based on their differences in age, texture, and mineralogy, i.e. Type I: Sungai Ara (southern part), and Type II: Bukit Bendera (northern part) (Tan 1994; Hashim et al. 2018) as shown earlier in Fig. 3. Type II is found in the southwestern (Batu Maung) part of the island. The main fault that passes from the north–south divides the island into two vertically. This fault extends to other areas like Tanjung Bunga, Paya Terubong, Tanjung Bunga, Air Itam, etc., that is perhaps one of the causes of periodic landslide situations in these areas shown in Table 2.

Materials and Methods

PS-InSAR technique has been applied for the detection of landslides and active landslide areas on the island of Penang in this work. The technique is a cost-efficient tool for remote sensing. It provides ground deformation measurements with high spatiotemporal resolution as compared to other conventional devices like Global Positioning System (GPS), Levelling, and Global Navigation Satellite Systems (GNSS) (Chen et al. 2017). The technique has been commonly used to measure the slow movement of landslides and applied to ground deformations measurement (Tong and Schmidt 2016; Chen et al. 2018). It is applied to process S-1A data in this study for ground deformation detection.

S-1A is one of the many image-capturing sensors operating in the C-band with a revisiting period of 12 days. It was launched on 3rd April 2014, by the European Space Agency (ESA) and operated in dual-polarisation (Navarro-Sanchez et al. 2014). It is a promising sensor in InSAR application due to its short revisit time (Haghighi and Motagh 2017). This mission offers four types of services,

namely Interferometric Wide (IW) Swath, Strip-map (SM), Wave (WV), and Extra Wide Swath (EW) with different polarisation conditions (Devanthéry et al. 2016), as shown in Table 3.

Similarly, ER method is a widely used method. It is an inexpensive, non-invasive, and fast method that generates appropriate information about subsurface settings. It is sensitive to the water content of the soil layers and good to examine potential landslide areas (Wu et al. 2018). The spatial distribution of resistivity in the subsurface is determined via the inversion model, which explains the electrical potential measured. There exist various types of methods, but the least square is commonly used. This approach offers a 2-D ground resistivity and allows identification of anomalies in the ground. Various applications of ER include studying weathering (Bièvre et al. 2016), investigating underground natural resources, and identification of the internal structure of various slopes deformations (Di Traglia et al. 2018).

As mentioned previously, this study used PS-InSAR, a ground motion detection tool, to track Penang Island landslides. The method relates slave scenes over the same region to one suitably chosen master. PSI-SAR is more flexible than traditional InSAR and had addressed the uncertainties that may be introduced to the results by atmospheric conditions on the radar pulses and ground reflectivity variation in ground vegetation or moisture content (Ferretti et al. 2000; Hung et al. 2011). The InSAR technique generally involves multiplication of two or more images of SAR to determine distances between the moving antenna and target area to get amplitude and phase information (Perrone et al. 2006). A radar system sends the signal to the surface of the earth where the antenna receives and records the backscattered signals from the target. The

Table 3 Mode of acquisition of Sentinel-1A data

Mode	Swath (km × km)	Geometric resolution (m)
Interferometric wide swath (IW)	250	5 × 20
Wave mode (WM)	20	5 × 5
Strip-map mode (SM)	80	5 × 5
Extra wide swath mode (WM)	500	20 × 40

two ways pulses between the radar and the calculated target area are called an interferogram that contains information about the stability of the surface of the earth (Lingyun et al. 2013).

The multi-temporal (MT) analysis was performed over the study area by exploiting the available dataset composed of a single look complex (SLC). The acquired 60 and 56 S-1A images on (20th February 2017, and 13th November 2019), and (1st September 2017 and 30th December 2018), from ascending and descending tracks were processed using SARPROZ software to measure, monitor, and map ground deformation in the study area. The S-1A data were acquired using Terrain Observation by Progressive Scans (TOPS) imaging mode operated by the ESA (Razi et al. 2018). The satellite used for data acquisition works in IW mode by passing over the area of interest (AOI) north to south in descending pass direction and south to north in ascending pass direction with 12 days revisiting cycles. In IW Swath Mode, data are acquired through a series of bursts with mutual overlaps by regular switching antenna beam between the sub-swaths (Roccheggiani et al. 2019). Table 4 presents some features of the S-1A dataset.

The first step was to create a project directory named SLC, in which the images downloaded were copied and stored. All the images were imported into the software, and appropriate AOI, such as latitude, longitude, and radius, shown in Table 5, were selected (Maghsoudi et al. 2018). The images acquired on 16th April 2018, and 29th March 2018, were chosen as the master images for the ascending and descending tracks, respectively, based on many crucial components such as fair-weather conditions, doppler vector, and normal temporal base (Perissin and Wang 2012; Razi et al. 2018; Luo et al. 2017). The images were later co-registered with the master images without any spatial

Table 4 Descriptions of the dataset of Sentinel-1A used for this research

Characteristics	Description
Launched	2014
Orbit	Near-polar
Centre frequency	5.405 GHz
Altitude	693 km
Polarisation	VV
Incident Angle	39
Revisit time	12 Days
Flight attitude	Right looking
Band	C
Revolutions per cycle	175
Wavelength	5.6 cm

Table 5 Subset of the dataset

Tracks	Longitude	Latitude	Radius (km)	Master Date
Ascending	100.1840	5.2651	21	20171111
Descending	100.1312	5.3209	18	20180329

errors to ensure that each target has azimuth and range geometry for master and slave scenes (Bakon et al. 2015) as depicted in the star graph of Fig. 4. The reflectivity map and amplitude stability index (ASI), sparse point selection mask, ground control points (GCP) selection, and external DEM and synthetic amplitude in SAR coordinate parameters were chosen for PS Candidates (PSC) (Declercq et al. 2017). Such steps offered opportunities for creating a map of reflectivity and displaying the DEM in the AOI. Due to the presence of additional noises associated with the hilly and vegetated areas, both the Goldstein filtering and multi-look (ML) modes were used to filter the data (Bakon et al. 2015). The images were geocoded to Google Earth and projected to 3-D orthophoto maps for the exportation of the results. The chart showing the processing of S-1A imageries using SARPROZ software is presented in Fig. 5.

The resistivity survey was done when the current electrodes were inserted into the ground, and the potential difference was measured through the potential electrodes. A dipole–dipole configuration was used as it offers good lateral resolutions as compared to other arrays such as Schlumberger and Wenner arrangements (De Bari et al. 2011; Wu et al. 2018; Kannaujiya et al. 2019). The set-up (Fig. 6a) includes ABEM Terameter SAS 4000, electrodes, cell, and reels of cable in the field. Two resistivity profiles were laid for imaging subsurface using 41 electrode poles with a spacing of 2.5 m. The data acquired were processed with the application of surfer software via computer iterations, where vertical 2-D resistivity contour maps were generated along the direction of the electrodes. The result was validated using Ahmad et al. (2014) borehole measurements.

Results and Discussion

The interferograms were generated from the 60 and 56 master–slave pairs of S-1A images acquired between 20th February 2017, and 13th November 2019, and from 1st September 2017 to 30th December 2018, for both the ascending and descending tracks, respectively, based on PS-InSAR technique. Due to the presence of additional noises associated with the hilly and vegetated areas, the

Fig. 4 Star graph network configuration of master and slave pair images of the Sentinel-1A time series. Each connection represents an interferogram (a phase difference map) considered to retrieve the SAR phase variation over time for each highly coherent ground target
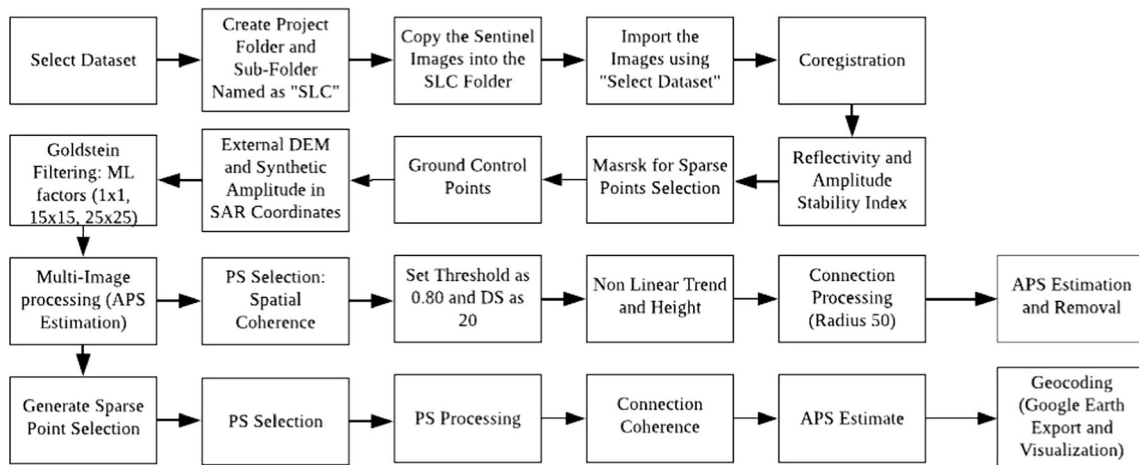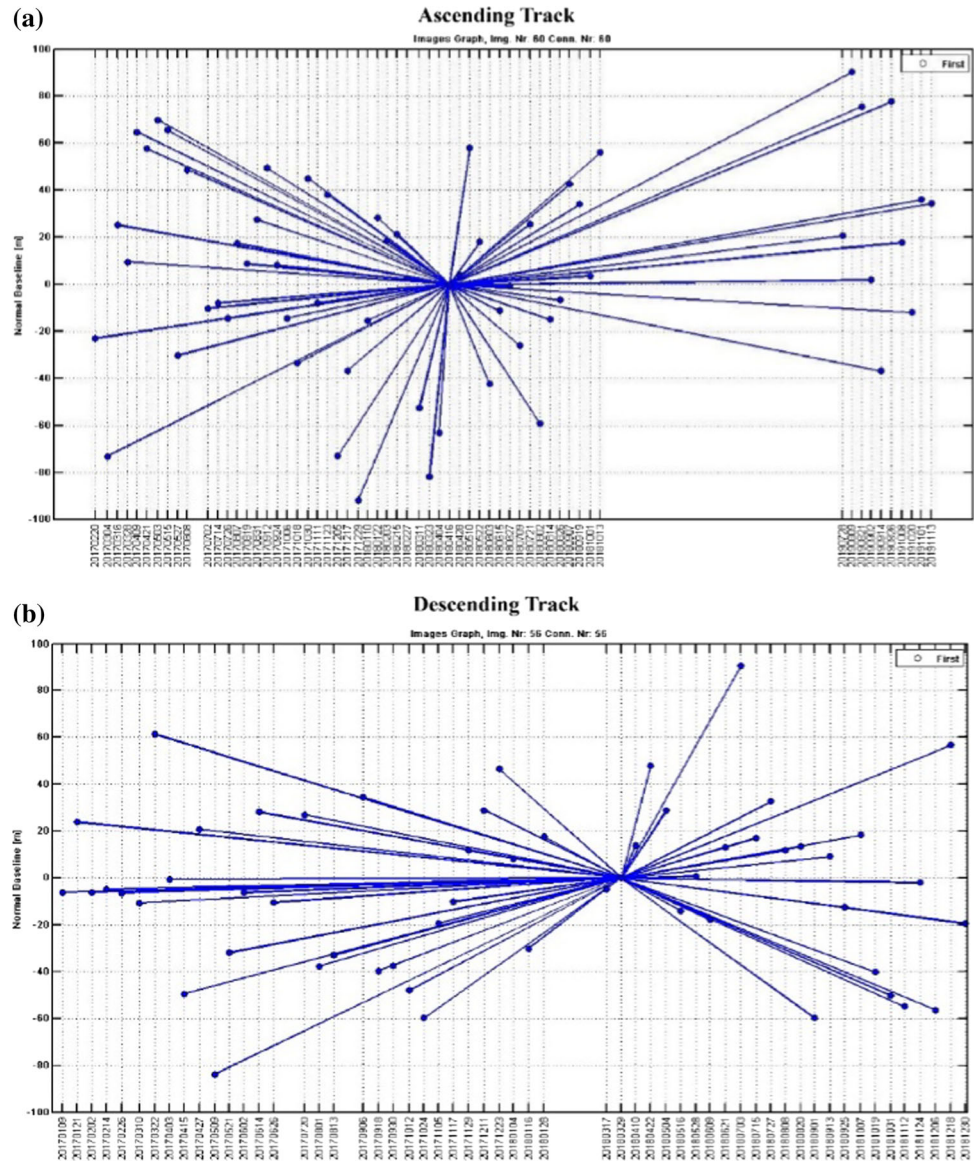

Fig. 5 Flowchart of the SARPROZ software for processing S-1A data

Fig. 6 Electrical resistivity set-up

multi-look factor and Goldstein filter were used to filter the data.

The quality of the generated interferograms depends on the temporal and normal baselines. It provides the ability to examine some smaller areas with significant problems of land deformation using ground deformation processing. A histogram graph shown in Fig. 7 is suitable for inspecting the isolated areas as it gives a better understanding of the statistical overview of connections coherence and information of PS points used for land displacements interpretations and analyses. The points values of 35,961 and 37,936 were obtained for the two tracks, respectively. These points were used to calculate the time series. The

linear trend and height correction between neighbouring PS candidates (PSC) was estimated by applying a temporal coherence histogram in the time domain after the estimation of all the parameters and APS removal. The number of PS points decreases with threshold values increasing. As illustrated in Figs. 3 and 6, Paya Terubong is situated in the centre of the island where extensive landslide tragedies had occurred.

Interest in unstable terrain identification increases as many neighbouring points display coherent and temporarily progressive motion. The ground displacement of the PS distribution points in the RGB colour scale is presented in Fig. 8a, where red points depict extreme movements with
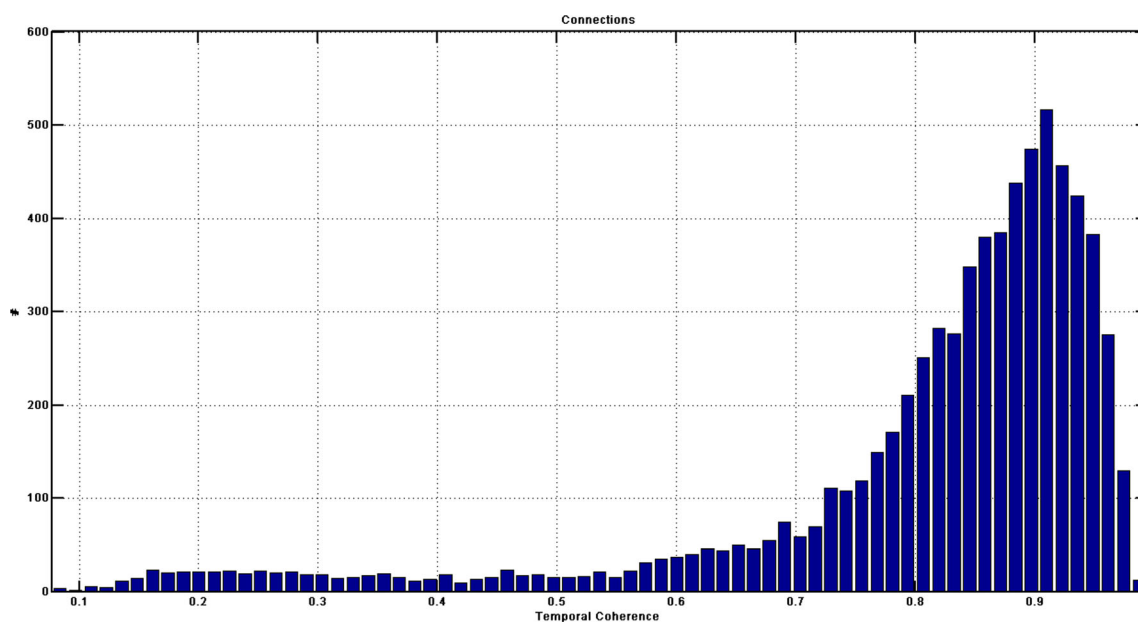
**Fig. 7** The temporal coherence histogram of points after parameter estimation and APS removal

the highest displacement and correspond to unstable targets showing vertical motions inferior to $\pm$ 12 mm/yr from the satellite LOS. The red dot band coincides with the areas of deformation where the instability is readily observable. Separate-colour points correlate with different PS displacement values and, many of these points are on an unstable slope amid the mountainous terrain. The figure generally shows that Penang Island area is globally unstable, where the blue colour connotes moderate displacement points throughout the study area and is used to discriminate movements beyond the observable background noise. The green colours denote stable points, whereas the densely distributed yellow points refer to the ground's vertical motion, representing unstable SAR backscattering targets positioned on stable terrain.

These results of PSI processing were geocoded and overlaid with the 3D orthophoto land mapping for validation and ground visualisation. The number of PS points increases as the threshold value decreases. From the InSAR processing, the coherence values of the PS points range from 0.2 to 0.65. The low value of this parameter is due to the presence of vegetation covers. The time series displacement for a PS point of Paya Terubong site is presented in Fig. 8b, where the x and y axes represent the temporal baseline in days and deformation value in millimetres, respectively. The movements exhibit linear motion ranging from − 1.5 to 41.3 90 mm/year away from a LOS of the system. The steep slope shows that there is a high acceleration of land movement. Different colours of the image correspond to a different displacement value of PS.

The results of the geoelectrical survey conducted to investigate the spatially varying ground movement about the geological setting of the affected area, as detected by the InSAR technique, are presented in Fig. 9. A significant contrast was not noticed from the results implying there are no geological discontinuities of the study area. The results only indicated some locations characterised by low resistivity values, which could be associated with the presence of water. In contrast, the high rate of resistivity may be related to the existence of underground events.

These results reflect the presence of underground water that typically alters the alluvial deposit, as shown in Fig. 9a and b. The observed low resistivity zone of 0–20 Ωm at a depth of up to 5 m at the study area coincides with the value of bedrock, according to the reports of (Ahmad et al. 2014). High resistivity values were observed at a depth of 5 m and above, indicating the presence of structurally shaped boulders (bedrock units) due to weathering and erosion (Ahmad et al. 2006). These results suggest that the bedrock units are situated at a depth of around > 5 m depth, the resistive layer is higher at greater depths. The gravelly terrace deposits of surveys (1 and 2) in Fig. 9 are imaged with two resembling layers having resistivity values between 3000 and 5000 Ωm. The data obtained using the dipole–dipole array, as seen in Fig. 6, are noted to be responsive to variations in lateral resistivity. Such variations are regarded as the ground deformation observed using the InSAR technique.

Fig. 8 Geocoded PS points on Google Earth and Time series of land deformation starting from 14th February 2017 to 1st September 2018 represented by PS point (ID 19641)
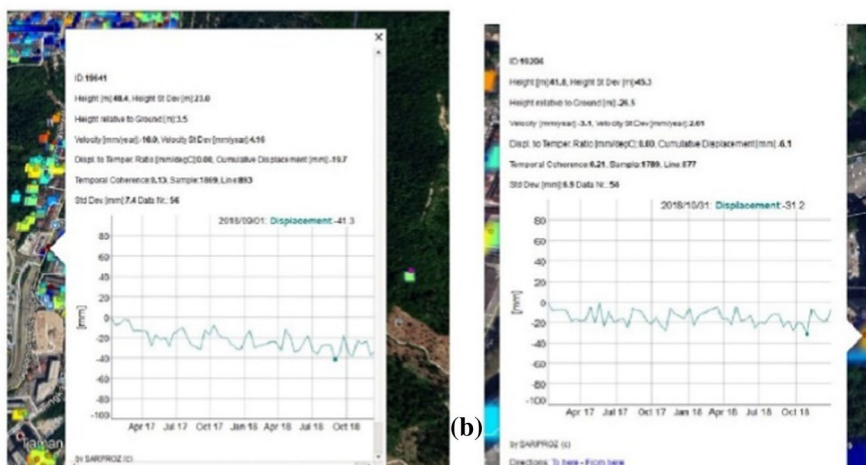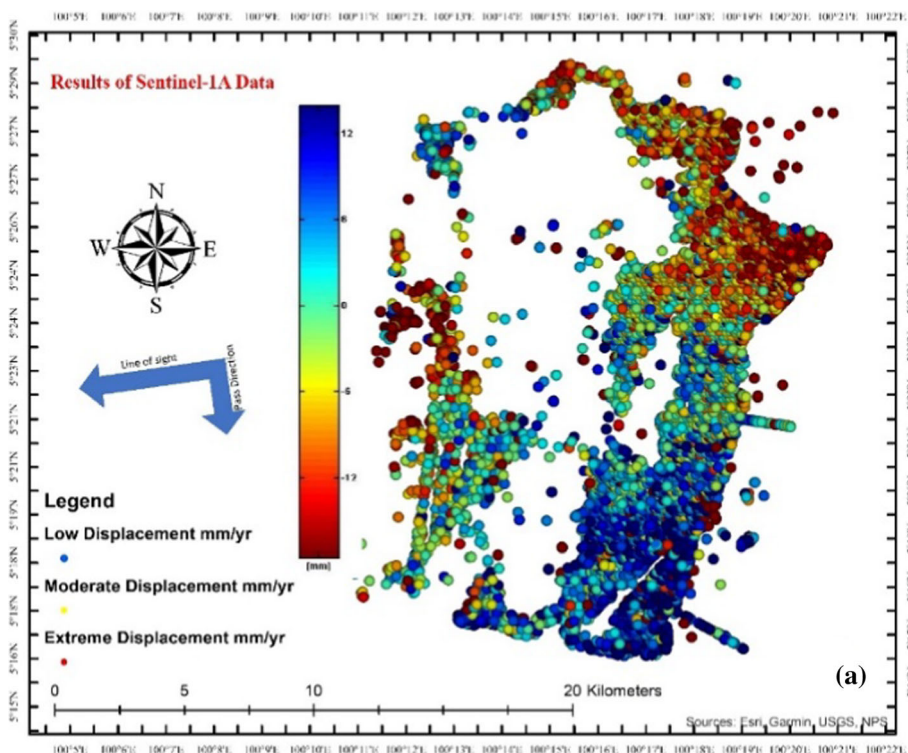
Discussion

It is evident from the overall results of PS-InSAR and ER that different factors influence the deforming areas investigated. The deformation pattern identified in Paya Ter-ubong is regarded as being due to the reactivation of past landslide phenomena. The tropical depression predicted by the South China Joint Typhoon Warning Center (JWTC) triggered a heavy rainfall that reactivated landslides located in a large region of Penang and Kedah and led to major disasters in those places (Meteorological Malaysia Department 2017). The observed ground deformation may be attributed to a landslide occurrence for which, however,

the only indication noticeable in the field and ER results could be related to the presence of very low resistivity values detected shown in Fig. 9. The knowledge of deformation mechanisms is summarised as probably attributable to human-made settlements on the ground. There can be no conclusive results on the origin of the deformation; however, the details presented by both PS-InSAR and ER techniques helps to predict a slow-motion subsidence phenomenon. The detected displacement could include, the shallow layer of unconsolidated sediment, which leans the conductive clay material. We cannot rule out the common triggering factors observed in the overall deformation processes. The findings of this study preclude
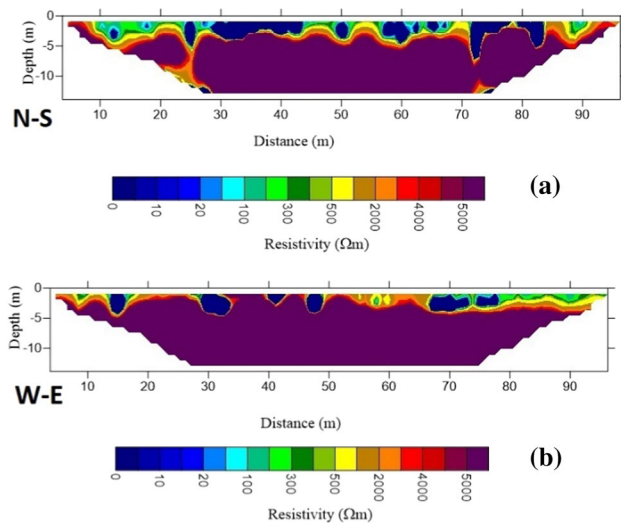
Fig. 9 The electrical resistivity results obtained with the dipole–dipole method (**a** represents line 1 and **b** depicts line 2)

us from having a definitive interpretation. The triggering factors on ground motions could include the shift in the geomorphological setting, subduction, sandy soils, and changes in groundwater levels besides those they have been previously mentioned.

Validation of Electrical Resistivity Results using Borehole Analysis

There is a need to validate the results of electrical resistivity while giving a detailed analysis. This validation was achieved with the application of borehole analysis of the study area.

Borehole logs collected from the Department of Public Works, Penang, in the work of Ahmad et al. (2014) were analysed and summarised to verify and validate the resistivity findings. The interpretations were based on the descriptive statistics of the thickness of sand and silt. Table 6 summarises the number of boreholes obtained, number of locations, and mean values of the thickness of both the sand and silt of the areas. In five areas, 112 borehole data were acquired from twelve different locations. The maximum sand thickness measured was attributed to its proximity to the sea, together with the area's

reclaiming activities. In Paya Terubong, the lowest silt thickness is 4.45 m. This value refers to the saturated areas, measured using the electrical resistivity method.

Conclusion

The past and potential ground deformation events in Penang Island have been monitored and mapped in this research with the application of the PS InSAR technique and electrical resistivity measurements.

The InSAR results suggested that the rate of landslides' magnitude is constant with a velocity of mm/yr. The areas with ground deformations (subsidence and uplift) were revealed through the InSAR technique, while the geophysical method revealed likely triggering mechanism in the subsurface. The results of this work are in line with previous studies to show that the middle of the island is vulnerable to landslides owing to its hilly terrain and dense forests. Paya Terubong remains the region that has had the most significant number of recent landslide occurrences in Penang Island.

The resistivity data obtained at a construction site located along the hillside in Paya Terubong were made possible, because the construction site had already deforested, flattened, and cleared the site for accessibility. Good results about the subsurface region were achieved from the 2-D resistivity data in which certain saturated locations were identified, examined, and interpreted. The aquifer was considered for areas with low resistivity values. Landslide events are also suspected as a result of certain boulder irregularities observed in the subsurface that may have developed as a result of weathering processes. These granitic boulders could be triggered by vibrations of pieces of machinery at the construction site even though mixtures are made a few metres away from the construction site.

Since there is no monitoring system in existence to study the dynamics of landslides in Penang and Malaysia as a whole, the integration of these two techniques is useful for landslide mapping and monitoring as it has comprehensive coverage with a high spatial resolution at a low cost. One single approach cannot be used as a stand-alone tool for solving landslide challenges in an urban area. The combination of the two techniques thus allowed the detection of

Table 6 Summary of the number of boreholes obtained, number of locations and mean values of the thickness of both the sand and silt in the study areas

Study Area	Boreholes	Locations	Mean value of thickness (m) Sand	Silt
Teluk Kumbar	25	1	3.38	8.15
Bayan Lepas	19	3	5.02	4.57
Paya Terubong	17	2	6.09	4.45
Batu Feringghi	26	4	6.05	6.49
Tanjung Tonkong	25	2	6.56	10.04

certain factors that could cause landslides in the region. This work can be used as a guide for detecting possible areas of landslides. The generated map will assist the government and contractors make suitable decisions in the expansion of Penang Island.

Authors' contributions KOR processed the data and prepared the manuscript. IAA downloaded the software and supervised the work and DP provided the technical support for the SARPROZ software used for the research.

Compliance with ethical standards

Conflict of interest The authors state that there is no conflict of interest regarding this manuscript's publication. Moreover, the authors have fully observed the ethical issues, including plagiarism, informed consent, misconduct, data manufacturing and/or falsification, double publication and/or submission, and redundancy.

References

Ahmad, F., Yahaya, A. S., & Farooqi, M. A. (2006). Characterisation and geotechnical properties of Penang residual soils with emphasis on landslides. *American Journal of Environmental Sciences, 2,* 121–128.

Ahmad, F., Yahaya, A. S., Halim, M. H., & Sian, K. C. (2014). Analysis of thickness of sand and silt in Penang Island. *Journal of Civil Engineering Research, 4,* 41–47.

Ali, M., Ahmad, F., Yahaya, S., & Farooqi, A. (2011). Characterization, and hazard study of two areas of Penang Island, Malaysia. *Human and Ecological Risk Assessment, 17,* 915–922.

Bakon, M., Papco, J., Perissin, D., Lazecky, M., Sousa, J. J., Hlavacova, I., et al. (2015). Monitoring of landslide activity in Slovakia territory using multi-temporal InSAR techniques. *European Space Agency, 731,* 8–12.

Bièvre, G., Jongmans, D., Goutaland, D., Pathier, E., & Zumbo, V. (2016). Geophysical characterisation of the lithological control on the kinematic pattern in a large clayey landslide (Avignonet, French Alps). *Landslides, 13,* 423–436.

Chee, S. Y., Othman, A. G., Sim, Y. K., Mat-Adam, A. N., & Firth, L. B. (2017). Land reclamation and artificial islands: Walking the tightrope between development and conservation. *Global Ecology and Conservation, 12,* 80–95.

Chen, F., Lasaponara, R., & Masini, N. (2017). An overview of satellite synthetic aperture radar remote sensing in archaeology: From site detection to monitoring. *Journal of Cultural Heritage, 23,* 5–11.

De Bari, C., Lapenna, V., Perrone, A., Puglisi, C., & Sdao, F. (2011). Digital photogrammetric analysis and electrical resistivity tomography for investigating the Picerno landslide (Basilicata region, southern Italy). *Geomorphology, 133,* 34–46.

Declercq, P. Y., Gerard, P., Pirard, E., Perissin, D., Walstra, J., & Devleeschouwer, X. (2017). Subsidence related to groundwater pumping for breweries in Merchtem area (Belgium), highlighted by Persistent Scatterer Interferometry. *International Journal of Applied Earth Observation and Geoinformation, 63,* 178–185.

Devanthéry, N., Crosetto, M., Cuevas-González, M., Monserrat, O., Barra, A., & Crippa, B. (2016). Deformation monitoring using persistent scatterer interferometry and Sentinel-1 SAR data. *Procedia Computer Science, 100,* 1121–1126.

Di Martire, D., Novellino, A., Ramondini, M., & Calcaterra, D. (2016). A-Differential synthetic aperture radar interferometry analysis of a deep seated gravitational slope deformation occurring at Bisaccia (Italy). *Science of the Total Environment, 550,* 556–573.

Di Traglia, F., Nolesini, T., Ciampalini, A., Solari, L., Frodella, W., Bellotti, F., et al. (2018). Tracking morphological changes and slope instability using spaceborne and ground-based SAR data. *Geomorphology, 300,* 95–112.

Ferretti, A., Prati, C., & Rocca, F. (2000). Nonlinear subsidence rate estimation using permanent scatterers in differential SAR interferometry. *IEEE Transactions on Geoscience and Remote Sensing, 38,* 2202–2212.

Furuichi, T., Osanai, N., Hayashi, S., Izumi, N., Kyuka, T., Shiono, Y., et al. (2018). Disastrous sediment discharge due to typhoon-induced heavy rainfall over fossil periglacial catchments in western Tokachi, Hokkaido, northern. *Landslides, 15,* 1645–1655.

Gin, O. K. (2015). Disparate identities: Penang from a historical perspective, 1780–1941. *Kajian Malaysia, 33,* 27–52.

Haghighi, M. H., & Motagh, M. (2017). Sentinel-1 InSAR over Germany: Large-scale interferometry, atmospheric effects, and ground deformation mapping. *ZFV Zeitschrift fur Geodasie, Geoinformation and Land management, 142,* 245–256.

Hashim, M., Misbari, S., & Pour, A. B. (2018). Landslide mapping and assessment by integrating Landsat-8, PALSAR-2 and GIS techniques: A case study from Kelantan State, peninsular Malaysia. *Journal of Indian Society and Remote Sensing, 46,* 233–248.

Hassan, N. M. K., Wahid, S., & Wahab, M. T. A. (2018). Geotechnical and minerology properties of marine clay at the northeast of Penang Island. *MATEC Web Conference, 203,* 1–11.

Hung, W., Hwang, C., Chen, Y., Chang, C., Yen, J. Y., Hooper, A., et al. (2011). Surface deformation from persistent scatterers SAR interferometry and fusion with leveling data: A case study over the Choushui river alluvial fan, Taiwan. *Remote Sensing of Environment, 115,* 957–967.

Kannaujiya, S., Chattoraj, S. L., Jayalath, D., Champati, R. P. K., Bajaj, K., Podali, S., et al. (2019). Integration of satellite remote sensing and geophysical techniques (electrical resistivity tomography and ground penetrating radar) for landslide characterization at Kunjethi (Kalimath), Garhwal Himalaya, India. *Natural Hazards, 3,* 1191–1208.

Kavzoglu, T., Sahin, E. K., & Colkesen, I. (2014). Landslide susceptibility mapping using GIS-based multi-criteria decision analysis, support vector machines, and logistic regression. *Landslides, 11,* 425–439.

Kundu, S., Saha, A. K., Sharma, D. C., & Pant, C. C. (2013). Remote sensing and GIS based landslide susceptibility assessment using binary logistic regression model: A case study in the Ganeshganga Watershed, Himalayas. *Journal of the Indian Society of Remote Sensing, 41,* 697–709.

Kwan, T. S., Krähenbühl, R., & Jager, E. (1992). Rb-Sr, K-Ar and fission-track ages for granites from Penang Island, West Malaysia: An interpretation model for Rb-Sr whole-rock and for actual and experimental mica data. *Contributions to Mineralogy and Petrology, 111,* 527–542.

Lingyun, J., Qingliang, W., & Shanlan, Q. (2013). Present-day deformation of Agung volcano, Indonesia, as determined using SBAS-InSAR. *Geodesy and Geodynamics, 4,* 65–70.

Luo, Q., Zhou, G., & Perissin, D. (2017). Monitoring of subsidence along Jingjin inter-city railway with high-resolution terraSAR-X MT-InSAR analysis. *Remote Sensing, 9,* 1–14.

Maghsoudi, Y., van der Meer, F., Hecker, C., Perissin, D., & Saepuloh, A. (2018). Using PS-InSAR to detect surface deformation in geothermal areas of West Java in Indonesia. *International Journal of Applied Earth Observation and Geoinformation, 64,* 386–396.

Meteorological Malaysia Department, 2017, Annual Rainfall Report. *Meteorological Malaysia Department* (pp. 1–90).

Mostafa, Y. E. S. (2012). Environmental impacts of dredging and land reclamation at Abu Qir Bay, Egypt. *Ain Shams Engineering Journal, 3,* 1–15.

Navarro-Sanchez, V. D., Lopez-Sanchez, J. M., & Ferro-Famil, L. (2014). Polarimetric approaches for persistent scatterers interferometry. *IEEE Transactions on Geoscience and Remote Sensing, 52,* 1667–1676.

Paradella, W. R., Ferretti, A., Mura, J. C., Colombo, D., Gama, F. F., Tamburini, A., et al. (2015). Mapping surface deformation in open pit iron mines of Carajás Province (Amazon Region) using an integrated SAR analysis. *Engineering Geology, 193,* 61–78.

Perissin, D., & Wang, T. (2012). Repeat-pass SAR interferometry with partially coherent targets. *IEEE Transactions on Geoscience and Remote Sensing, 50,* 271–280.

Perrone, A., Zeni, G., Piscitelli, S., Pepe, A., Loperte, A., Lapenna, V., et al. (2006). Joint analysis of SAR interferometry and electrical resistivity tomography surveys for investigating ground deformation: The case-study of Satriano di Lucania (Potenza, Italy). *Engineering Geology, 88,* 260–273.

Pradhan, B., & Lee, S. (2010). Delineation of landslide hazard areas on Penang Island, Malaysia, by using frequency ratio, logistic regression, and artificial neural network models. *Environmental Earth Sciences, 60,* 1037–1054.

Razi, P., Sumantyo, J. T. S., Perissin, D., Kuze, H., Chua, M. Y., & Panggabean, G. F. (2018). 3D land mapping and land deformation monitoring using persistent scatterer interferometry (PSI) ALOS PALSAR: Validated by Geodetic GPS and UAV. *IEEE Access, 6,* 12395–12404.

Roccheggiani, M., Piacentini, D., Tirincanti, E., Perissin, D., & Menichetti, M. (2019). Detection and monitoring of tunneling induced ground movements using Sentinel-1 SAR interferometry. *Remote Sensing, 11,* 1–14.

Schulz, W. H., Coe, J. A., Ricci, P. P., Smoczyk, G. M., Shurtleff, B. L., & Panosky, J. (2017). Landslide kinematics and their potential controls from hourly to decadal timescales: Insights from integrating ground-based InSAR measurements with structural maps and long-term monitoring data. *Geomorphology, 285,* 121–136.

Tan, B. K. (1994). Engineering properties of granitic soils and rocks of Penang Island, Malaysia. *Bulletin of the Geological Society of Malaysia, 35,* 69–77.

Tappenden, K. M. (2014). The district of north Vancouver's landslide management strategy: Role of public involvement for determining tolerable risk and increasing community resilience. *Natural Hazard, 72,* 481–501.

Tong, X., & Schmidt, D. (2016). Active movement of the cascade landslide complex in Washington from a coherence-based InSAR time series method. *Remote Sensing of Environment, 186,* 405–415.

Virk, A. S., Singh, A., & Mittal, S. K. (2019). Monitoring and analysis of displacement using InSAR techniques for Gulaba landslide site. *Journal of Engineering Science and Technology, 14,* 1558–1571.

Wilkinson, P. B., Uhlemann, S., Chambers, J. E., Meldrum, P. I., & Loke, M. H. (2014). Development and testing of displacement inversion to track electrode movements on 3-D electrical resistivity tomography monitoring grids. *Geophysical Journal International, 200,* 1566–1581.

Wu, Z., Wang, X., Chen, Y., Cai, Y., & Deng, J. (2018). Assessing river water quality using a water quality index in Lake Taihu Basin, China. *Science of the Total Environment, 612,* 914–922.